Supplementary Information:

Ultrafast Neuromorphic Computing Driven by Polariton Nonlinearities

Yusong Gan[1,†] , Ying Shi[1,†], Sanjib Ghosh[3,2], Haiyun Liu[2], Huawen Xu[2,*], Qihua Xiong[1,2,4,5,*]

[1]State Key Laboratory of Low-Dimensional Quantum Physics and Department of Physics, Tsinghua University, Beijing, 100084, P.R. China.

[2]Beijing Academy of Quantum Information Sciences, Beijing, 100193, P.R. China.9

[3]School of Science and Engineering, The Chinese University of Hong Kong, Shenzhen, Shenzhen 518172, P. R. China.

[4]Frontier Science Center for Quantum Information, Beijing, 100084, P.R. China.

[5]Collaborative Innovation Center of Quantum Matter, Beijing, 100084, P.R. China.

[*]Corresponding author(s). Email(s): xuhw@baqis.ac.cn; qihua_xiong@tsinghua.edu.cn

[†]These authors contributed equally to this work.

Table of Contents

I. Details on $FAPbBr_3$ growth

We developed solution-limited growth, where physical confinement and low-temperature solution synergistically regulate the controlled preparation of large-area, high-quality $FAPbBr_3$ single-crystal films. The core design of this method includes four main steps:

1. **Hydrophobic Interface Modification**: First, substrates such as SiO2/Si, sapphire, and quartz are ultrasonically cleaned with acetone, ethanol, and deionized water for 15 minutes and dried with nitrogen. Subsequently, a 50 W power, 10-minute oxygen plasma treatment is applied. The plasma-cleaned substrates are then modified with octadecyl trichlorosilane (OTS, 99%) using vapor deposition, resulting in a hydrophobic surface. After OTS treatment, the surface energy of the substrates is reduced, minimizing the non-specific adsorption of precursors on the surface, thus forcing nucleation to occur only within the confined space and improving the orientation consistency of the single crystals.
2. **Low-Temperature Solution Nucleation Control**: Methylammonium bromide (FABr) and lead bromide (PbBr2) are dissolved in a DMF and γ-butyrolactone mixed solvent (volume ratio 2:3) at a 1:1 molar ratio, forming a 1 M FAPbBr3 precursor solution. The viscosity and evaporation rate of the solution can be adjusted by modifying the solvent ratio.
3. **Confined Space Construction**: Two hydrophobically treated substrates (e.g., OTS-modified SiO2/Si) are placed face-to-face with a controllable gap, forming a uniform slit-like confined space. Then, 0.9 μL of the supersaturated precursor solution is dropped onto the edges of the two substrates, and capillary action causes the solution to spontaneously infiltrate the gap, restricting its lateral diffusion and forcing crystal growth in a two-dimensional plane.
4. **Pressure-Assisted Crystallization**: The substrates are placed at the center of a custom fixture, applying a weight of approximately 280 kg. The entire assembly is placed on a 65°C constant temperature heating plate and allowed to stand for 36-48 hours. Finally, a perovskite single-crystal film grows on the OTS-modified substrate.

By controlling the applied uniform pressure with the custom fixture, the thickness of the film can be controlled.

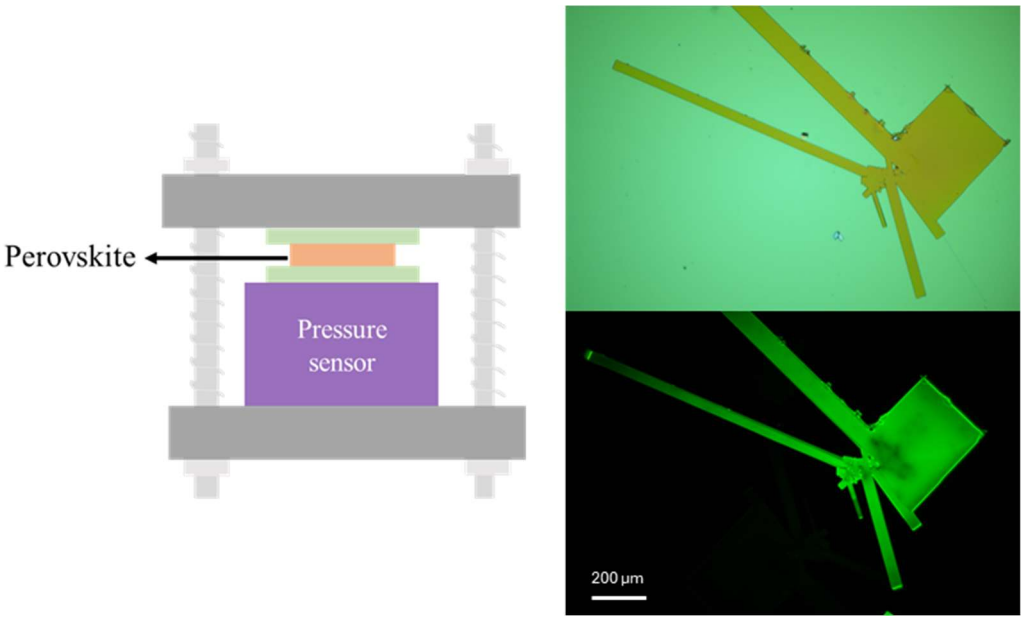

Figure S1: Sample growth, device(left) and images(right)

The XRD, absorption, and photoluminescence spectra of perovskites grown using this method can be referenced from our group's previous work[1,2].

II. Details of pattern generation with SLM

In this experiment, we used a spatial light modulator (SLM) to encode the input information. The SLM model is the 1920×1200 XY Phase Series Spatial Light Modulator with an HDMI controller from Meadowlark Optics. It has a 1920×1200 adjustable pixel array, with each pixel measuring $8\,\mu m \times 8\,\mu m$. Considering the overall magnification of the optical setup and the aperture of the objective lens, we encoded only the central 800×800 region of the SLM. After passing through the optical system, the encoded pattern was focused onto the sample. This process can be regarded as a Fourier transform of the input optical field. In the Fourier plane (also 800×800), after calibration using a calibration scale, each pixel corresponds to a final

size of $0.2\,\mu m$ on the sample. The images from our dataset were placed within a $20\,\mu m \times 20\,\mu m$ central region and were ultimately collected by the spectrometer.

Since our spatial light modulation can only control the phase delay introduced by the liquid crystal array, it cannot directly manipulate the intensity distribution of the pattern. Therefore, we employed the Gerchberg–Saxton algorithm in combination with a lens system for far-field imaging. The Gerchberg–Saxton algorithm is a classic iterative method for holographic imaging, which can be simplified into the following process:

$$N_i = FFT(Amplitude(Source) \cdot e^{i \cdot Phase(M_i)})$$

$$M_{i+1} = iFFT(Amplitude(Target) \cdot e^{i \cdot Phase(N_i)})$$

Here, Source and Target represent the intensity distributions (patterns) of our light source and target, respectively. M and N denote the complex fields (amplitude with phase) in the real plane and Fourier plane at each iteration. FFT and iFFT refer to the Fourier transform and inverse Fourier transform, respectively. By superimposing the phase matrix computed via the Gerchberg–Saxton algorithm with a grating phase, the zero-order beam can be filtered out, enabling high-quality image information encoding (see Fig. 3a in the main text). Below is an example of a phase matrix calculated using this method, representing the pattern of the number "5".

It is worth noting that due to instrument precision limitations, the generated patterns are not entirely identical to those in the original MNIST dataset. To eliminate the influence of this factor on the experiment, we directly captured the excitation light patterns and trained the model following the steps outlined in the main text. The accuracy achieved was only 80%, lower than the 85% obtained with the standard MNIST dataset used as a reference. This result rules out the impact of SLM encoding on the outcome. Therefore, in the main text, we still use the higher accuracy as our reference.

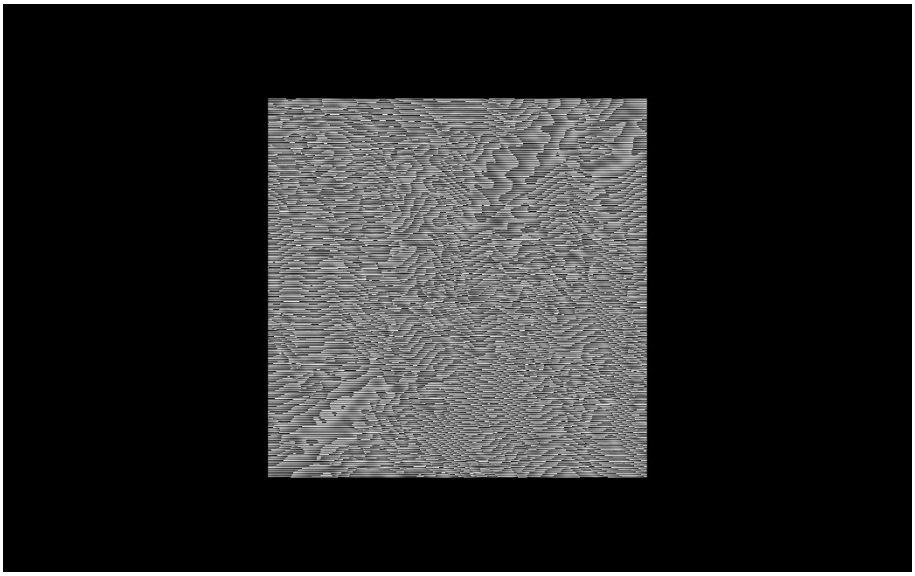

Figure S2: An example phase diagram of a digit image, from dark to bright represents a phase range from 0 to 2π

III. Details of dataset preparation

For the MNIST dataset, its standard size consists of 60,000 training samples and 10,000 test samples. In our experiments, we selected 1,000 samples for small-scale testing. To prevent bias in training accuracy caused by dataset selection, we followed randomization principles during both dataset selection and measurement processes. First, we shuffled the order of all 70,000 images, then randomly selected 1,000 images with their corresponding labels for our experiment. This random selection was performed only once, meaning all subsequent tests were conducted using the same fixed dataset. These selected data were encoded and re-shuffled before being tested on our device, yielding 1,000 output matrices along with their true labels.

To ensure experimental results remained unaffected by variations in experimental conditions, we further divided this 1,000-sample dataset into training and test sets using a 9:1 ratio through random partitioning. This approach approximately ensured uniform distributions across both sets. As shown in Table S1, statistical analysis of ten different partition trials demonstrates comparable occurrence probabilities for each digit

category in the test sets. Using ridge regression on the 900-sample training set, we obtained our weight matrix W. This matrix was then applied to predict the 100-sample test set, with predictions compared against actual labels (an example is illustrated in Fig. 3c of the main text). Considering the inherent randomness in test set selection, we repeated this partitioning process ten times. Each distinct partition generated corresponding accuracy results, ultimately enabling us to compute the mean accuracy and standard deviation through statistical analysis.

To ensure that the 100 test images accurately reflect trends in accuracy variation, we supplemented the evaluation with an expanded dataset. The selection method mirrored the previous approach, but the test set was enlarged to 400 samples. Building on this, we randomly extracted subsets of varying sizes from the 400 test samples to assess how test set size impacts accuracy outcomes. As demonstrated in Figure S3, increasing the test set size gradually reduced the standard deviation of accuracy from 0.7% to below 0.5%, while the mean accuracy remained relatively stable. This observation indirectly validates the reliability of the data.

Testing digits	0	1	2	3	4	5	6	7	8	9
Power 1	11	11	10	10	11	9	10	10	8	10
Power 2	10	8	11	11	9	12	11	10	10	8
Power 3	12	8	9	11	9	10	8	12	8	13
Power 4	7	11	12	9	10	9	9	11	10	12
Power 5	10	8	8	11	9	12	12	13	9	8
Power 6	8	12	9	9	12	8	9	12	10	11
Power 7	10	10	9	9	11	9	9	10	11	12
Power 8	10	9	8	9	11	11	8	12	10	12
Power 9	11	10	11	9	11	10	9	11	9	9

Table S1: Sampling of the digit distribution in the test set

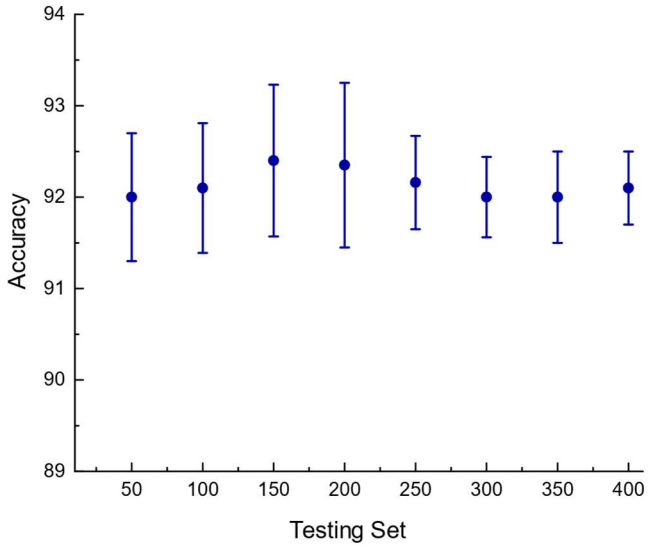

Figure S3: The classification accuracy as a function of testing set size, with error bars representing the standard deviation from 10 randomly selected testing sets.

Reference

1 Chen, Y. Z. *et al.* Unraveling the Ultrafast Coherent Dynamics of Exciton Polariton Propagation at Room Temperature. *Nano Letters* **23**, 8704-8711 (2023).

2 Shi, Y. *et al.* Coherent optical spin Hall transport for polaritonics at room temperature. *Nature Materials* **24**, 56-62 (2025).